The University of North Carolina at Chapel Hill

Senior Honors Thesis

Department of Physics and Astronomy

Synthetic Image Production for Digital Chest Tomosynthesis

Author:
Alexander Morrow

Thesis Advisor:
Dr. Otto Zhou

April 9, 2022

Contents

Acknowledgments

I would like to award a number of thanks to those who have helped me along my undergraduate journey and research to this point. Firstly, I would first like to thank Dr. Otto Zhou, my research adviser, for his guidance over the course of my medical physics research journey. Without his insights, I would not know as much as I do about the world of medical physics. Further, I would like to thank Dr. Christy Inscoe, a member of the Zhou laboratories, for her support in the development of this thesis, providing the DICOM images used throughout, and her presence throughout my research career. Without her presence, I would not contain as much joy in the research that I do now. Special thanks is also to be awarded to Dr. Connor Puett for providing the base MATLAB code on which this project operates. Without his dutiful work, completing a project of this scope would have been significantly more difficult within the given time span of research. I would also like to thank my father and mother Christopher and Sarah Morrow, as well as my younger siblings Anna, Katelyn, Ashley and Joshua Morrow, for their love and unending support over the course of my entire academic career. Without my family behind me, I would not be half the person I am today, for which I am and will forever be grateful for. Finally, I thank the Department of Physics and Astronomy at The University of North Carolina at Chapel Hill, along with all of my friends and fellow student researchers, for curating my knowledge in the field of physics itself and refining it into something amazing. Without all of the professors, peers, friends, and others who have helped me along over the course of my undergraduate career, I would not have such an extensive amount of knowledge in all of the fields which I have been given the opportunity to study. My thanks to you all is as immeasurable as the support you have provided me.

Honor Code

On my honor as a student of The University of North Carolina, I certify that I did not lie, cheat, steal, or receive any unauthorized aid while completing this honors thesis and did not encourage the use of nor give any unauthorized aid to others in the completion of this honors thesis.

Signature: _____

Alexander Morrow, Class of 2022

Preface

It was not until my freshman year of college that I heard of the field of medical physics. Of course, I was quite familiar with each individual word prior to that point, but I had never considered it to be possible to put them together in such a way. Since I could work I was involved with the medical field, providing direct support and care to individuals at nursing homes and immediate care facilities for individuals with intellectual disabilities (ICF-IID homes), and I took college-level physics courses in high school, yet I never heard of medical physics. Admittedly, I was immediately smitten with the very concept of medical physics when two of my professors for an introductory physics course offhandedly mentioned such research being performed at Chapel Hill. That same day, I furiously searched the web for this medical physics, and found an entire world's worth of knowledge. I read on in awe of all the things that, unbeknownst to me, spoke to one of my deepest desires of combining my love for the sciences, mathematics, and medicine in such a unique way all into one career field, my dream job. It was at that moment that I decided to change my degree path into physics, and pursue a career as a medical physicist.

A year following that decision, I joined the Zhou laboratories and have advanced my knowledge in medical physics considerably. In such a short time it feels, I had learned so much about the many interconnecting parts which constitute the life of a medical physicist, from research to financing to project defenses, my appreciation for the field grew daily, but so did my worries. It felt at times overwhelming, too daunting of a field to involve oneself in and too abstract of a task to complete for each project I involved myself with, and becoming overwhelmed would impact my own ability to do research. There was always an undercurrent of hesitation I took with each task presented to me, a sort of doubt that I would not understand what I needed to accomplish and would disappoint the advanced researchers who put their trust in my abilities. What it was that pushed me through each day of overwhelming doubt and disappointment in myself, was a reminder of that very day I first learned about medical physics, of that awe and wonder I felt at this world of science applied in such a unique and helpful way, in the way that I always wanted to help others.

This honors thesis serves, certainly, as a culmination of all that I have learned from my time as an undergraduate researcher, a testament to that which I have accomplished under the tutelage of the Zhou laboratories. While I write this paper though, I cannot help but think of the younger man I once was who, simply from a passing comment, changed his entire field of study for something he believed he would enjoy all the more. It is for that younger man, and for any and all people who might hold that same desire I once had in medical physics, that I write this honors thesis for as well. It is written to be accessible to any person interested in learning about synthetic image production applied to medical physics, and to those who already know much about it. I hope that, by writing this honors thesis, I may help cultivate any of the curious minds which may desire to learn more about what it is that may constitute the world of medical physics, from an aspiring medical physicist themselves.

1 Introduction

> The measure of greatness in a scientific idea is the extent to which it stimulates thought and opens up new lines of research.
>
> *P.A.M. Dirac* [1]

1.1 Abstract

The focus of this thesis is on the process of developing synthetic images from a digital chest tomosynthesis scan and evaluating the quality of the synthetic images for five patients using this process. Results demonstrate that the outlined PRIISM method is capable of producing intelligible synthetic chest images when compared to chest radiographs of the same body. The full-stack synthetic images possess high in-plane resolution with expected lacking depth resolution but often included numerous bright spots, low body coverage, and heightened bone presence. Slabbing the synthetic images removed most bright spots prominent in the full stack synthetic images and reduced rib bone presence over the lungs, but decreased the in-plane resolution and highly contrasted rib bones along the left and right edges of the lungs. Avenues for further evaluations of the quality of PRIISM, including ROC curve analysis and 3D simulation of the tomosynthesis data for viewing at various angular coverages, are discussed.

1.2 Historical Background

It is the prevailing consideration that the study of medical physics was born in the year of 1895 with Wilhelm Conrad Röntgen's observation of a form of electromagnetic radiation generated from cathode radiation studies that, when impinging on photographic plates, made the material fluoresce [2]. The discovery of this unique form of electromagnetic radiation, what were once called Röntgen rays and are now referred to as X-rays, would net Röntgen the first Nobel Prize in Physics in 1901. The wide applicability of X-rays to other fields of research, chief among them being medicine, was made apparent after Röntgen released one of the first, and perhaps the most famous, images produced from X-rays: a scan of his wife's hand, as shown in Fig. 1.

Figure 1: The "Hand mit Ringen," (literally, hand with rings) one of the first ever X-ray scans performed, shown is Anna Bertha Ludwig's hand. The large mass concentration on the 4th finger's proximal phalanx is Ludwig's ring, which she wore during the scan [3].

It comes as no surprise as to *why* there would be such an interest in the newly-found X-rays in the medical field: medical professionals could observe the inner workings of the human body via noninvasive means. Within days of Röntgen's published discovery of the X-rays, doctors were producing radiographs to demonstrate its potential applications in dental work, and within a year X-ray images were being produced to help gunshot victims [4].[1] The use and application of X-rays would expand into and create new and unique fields of research over the next 100 years, but its usage in the field of medicine is almost decidedly the most important consequence of X-rays to date.

Multiple different imaging techniques have been developed since the advent of X-rays to maximize the information gained from images produced while minimizing the plethora of issues that come with the practice of X-ray imaging including, but not limited to: uncomfortable or painful positioning of body parts preceding and during the active imaging phase, radiation exposure, energy required to power the source and scanning device, and lackluster image reconstruction techniques [5]–[12]. Computed tomography (CT) is one such technique, where an X-ray source is rotated about the body of a patient and can produce images at different angles of a bodily region of interest, with the imaging information being processed by a computer. Digital tomosynthesis (DT) is another such technique, similar to CT where one takes sectional images of the human body and reconstructs them into images via digital analysis. Comparing the two, modern DT offers a number of advantages over modern CT: reduced

[1] It is unfortunate to note that most of these medical professionals, including those producing the devices which could produce X-rays, the X-ray tube, and those patients being irradiated, would suffer greatly from prolonged radiation exposure [4].

rotation of the source-detector setup over the imaging surface, fewer sectional images required to create a reconstructed image, reduced radiation exposure, and generally being more cost effective [13]–[20].

The foundation of digital tomosynthesis can be attributed to the Dutch researcher Bernard George Ziedses des Plantes who, in 1932, developed a device where an X-ray tube and an image receptor moved simultaneously over an anatomical region that produced multiple thin layer image slices of the region that could highlight small abnormalities otherwise overlooked in larger-slice imaging [21], [22]. Ziedses des Plantes named the method of image acquisition tomography, for each of the images taken in a selected plane of the anatomical region filled the same position while regions outside of the selected plane were blurred and unfocused. While the device and method Ziedses des Plantes offered to the medical community had the potential to characterize small masses previously undetectable, it did not come without notable issues: the method of image acquisition presented by Ziedses des Plantes was complex, multiple procedures would have to be run to produce more than a single slice which brought increased risk of high X-ray exposure, and it proved difficult to suppress multiple details coming from outside of the select plane of interest from projecting into the final image [21]–[23]. It would take until 1969 for Ziedses des Plantes' work to be commercially implemented, the "three-dimensional roentgenography" developed by Garrison *et al* could produce a 3D image from one scan and reduce much of the issues initially found with Ziedses des Plantes' tomography apparatus [21], [24]. Even with the new findings and advancements made by Garrison *et al*, DT would lose traction in the medical field with the advent of CT technology in the 1970s, spearheaded by scientists Sir Godfrey Hounsfield and Allan Cormack.[2] The revolution that was CT technology shifted focus from improving DT technology, to implementing CT technology in hospitals and research laboratories.

1.3 Motivation of Study

To call the resurgence of DT application and study in the modern medical world a revival would undermine its usage: even with the significant rise in popularity that CT technology brought with it, the study of DT never ended [25]–[28]. Rather, its momentum has been building slowly with the refinement of the technology over time, with new avenues of study becoming viable. Digital breast tomosynthesis (DBT), for instance, is an FDA-approved method of screening for breast cancer alongside standard mammography and has demonstrated higher sensitivity for detecting cancers and a decreased false-positive rate when compared to mammography [29]. Digital chest tomosynthesis (DCT) is another burgeoning subclass of DT, focusing on imaging parts of the body that reside within the chest - objects such as the lungs or the heart - and detecting potential abnormalities. DCT has been studied for its applicability in identifying

[2]Their work would lead to them receiving the Nobel Prize in Physiology or Medicine in 1979.

and tracking the progress of cystic fibrosis in patients through the detection of bronchiectasis, mycobacterial infections, and lung cancer with the characterization of lung lesions and nodules, along with the potential of DCT to be used in conjunction with chest radiography [17], [19], [30]–[32]. Given the current state of the COVID-19 pandemic, investigations have also been made on the application of DCT images in clinical settings for detecting COVID-19 and its variants [33], [34]. Furthering the understanding of DCT and demonstrating its applicability as an alternative or supplement to current chest imaging modalities can provide those same aforementioned general benefits of DT: reduced radiation exposure, shorter procedure length, and being cost-effective. Multiple different avenues are available to test the potential improvements that DCT can offer: apparatus design, X-ray production and geometries, projection and reconstruction algorithms, and various others.

2 Theoretical Background

> E'en hell hath its peculiar laws, I see!
>
> *Johann Wolfgang von Goethe* [35]

2.1 The Radon Transform and Filtered Back Projection

The mathematical background to which most medical imaging, in particular tomography, can be attributed is to the work of Johann Radon. By 1917, Radon devised a method for taking the information gained from a material that projected through some object, for tomosynthesis it being the data taken from X-rays passing through some bodily structure and reshaping it to highlight characteristics inside of the object [36]. The full treatment of Radon's work is lengthy, presupposes an understanding of various complex mathematics, and altogether deserving of an honors thesis to be completed on it. Therefore, I shall limit myself to discussing only the most relevant information necessary to comprehend the underlying physics and mechanics of DT, relying heavily on the theses [37]–[39] from which a full discussion on Radon's work can be read, Radon's original work in [36], and only working through the 2-dimensional case.

We start by making a select number of assumptions about a hypothetical setup in which one performs a parallel-beam X-ray scan on some object:

1. The X-ray beams are not subject to the effects of refraction and diffraction - they do not scatter nor bend when they encounter a surface.
2. The X-ray beams are monochromatic - the photons are of a single energy and propagate at the same frequency.
3. The X-ray beams are infinitesimally wide and emanate from an X-ray source, which for each beam acts as a point source.
4. We can define some function $f(P)$ for all real points $P = [x, y]$, in which $f(P)$ is continuous.
5. Eq. 1, extending over the whole real plane, is continuous:
$$\iint_{\mathbb{R}^2} \frac{|f(x,y)|}{\sqrt{x^2+y^2}}\,dx\,dy. \tag{1}$$
6. For any arbitrary point P and each $r \geq 0$ we can define the average function:
$$\overline{f_P}(r) = \frac{1}{2\pi}\int_0^{2\pi} A(x + r\cos\phi, y + r\sin\phi)\,d\phi, \tag{2}$$
such that for every point P,
$$\lim_{r\to\infty} \overline{f_P}(r) = 0. \tag{3}$$

Whenever X-rays pass through a medium, what is conventionally called the absorber, the intensity of the traversing ray can be reduced as the photons are scattered, diffracted, absorbed, or otherwise interacted with by the absorber, a process known as attenuation. Now we enforce condition 1, where the attenuation is only a consequence of absorption by the absorber. As it has been demonstrated that the ability of an absorber to reduce the intensity of a traversing X-ray is primarily due to the absorber material, this is a fair assumption to make [40]–[42]. Enforcing condition 2, we find that the strength of a medium to attenuate X-rays is given in the form of the linear attenuation coefficient $\mu(x)$, determined experimentally using the Lambert-Bouguer law of absorption:[3]

$$I(x) = I_0 e^{-\mu(x)\cdot x}, \tag{4}$$

where $I(x)$ is the transmitted X-ray intensity at depth x, and $I_0 = I(x_0)$ is the initial X-ray intensity at position x_0 [42]. We can also define the mass attenuation coefficient, given as the linear attenuation coefficient per unit density of the medium ρ, which allows us to write Eq. 4 as

$$I(x) = I_0 e^{-\left(\frac{\mu(x)}{\rho}\right)\rho\cdot x}. \tag{5}$$

As it will become relevant, we can also write Eq. 4 in the form

$$\ln\left(\frac{I_0}{I}\right) = \int_{x_0}^{x} \mu(x')\, dx', \tag{6}$$

with I being the final intensity at depth x.

We begin by shifting our coordinate system into one where we can handle lines of an infinite slope, which Cartesian coordinates handle poorly, by normal line parameterization as required by condition 3. Consider a rotation θ onto the axis s, effectively treating the quantity s as an arc length; by defining the quantity $t = x\cos\theta + y\sin\theta$, a consequence of the normalization of our values over a unit circle, the parameterization can be completed via the rotation matrix $\mathbf{R}$:

$$\begin{bmatrix} x(s) \\ y(s) \end{bmatrix} = \mathbf{R}\begin{bmatrix} t \\ s \end{bmatrix} = \begin{bmatrix} \cos\theta & -\sin\theta \\ \sin\theta & \cos\theta \end{bmatrix}\begin{bmatrix} t \\ s \end{bmatrix} = \begin{bmatrix} t\cos\theta - s\sin\theta \\ t\sin\theta + s\cos\theta \end{bmatrix} \tag{7}$$

Now enforce conditions 4-6 onto our system, meaning it has compact support.[4] It is now prudent to explain what we wish to *do* with all that we have. Recall the hypothetical experimental setup: we have a parallel-beam X-ray scan being performed on some object. The X-ray source moves around the scanned object with a detector on the other side of the object. As the incident X-rays pass through the scanned object they are attenuated to varying degrees depending on what they interact with, so the outputted intensity is different for each

[3] One may be quick to correct this to the Beer-Lambert-Bouguer law, yet note that only the path length and intensity of the incident X-ray are named. See Lambert's original work in [43].

[4] See [36] for the full mathematical implications of compact support. Simply put, the slice image information produced is finite and does not span the entire space in which we work.

transmitted beam. If we wish to know the intensity density of the X-rays which impinge upon the detector surface at one location, then we must sum over the entire detector length the attenuations of each beam. Given strict enforcement of condition 3, we have beams of infinitesimal width that cover an infinitesimal portion of the detector region, so it is sensible to instead consider the summation as an integral over the entire space by infinitesimal length segments along the face of the detector. Under the conditions that $t \in \mathbb{R}$, $\theta \in [0, 2\pi)$ and that $\mu(t, \theta) \in \mathbb{R}^2$, this can be summarily written as:

$$S(t, \theta) = \mathscr{R}\mu(t, \theta) = \iint_{\mathbb{R}^2} \mu(x, y)\, dx\, dy. \tag{8}$$

Eq. 8 is the Radon transform of μ, written as $\mathscr{R}\mu$. Note the similarity Eq. 8 has to Eq. 6. This is no mere happenstance: the Radon transform of μ is the measured intensity data. The function $S(t, \theta)$ is often called a sinogram due to the characteristic sinusoidal shape produced by a point-source object. Some unique properties of the Radon transform are that it is a linear and even transform.[5]

Eq. 8 can be written in different forms by utilizing various properties. Consider the parallel-beam configuration: if we measure the intensity density of the X-ray beams as the contribution of each of these infinitesimally-small X-ray beams, effectively lines, along the face of a detector, then we can instead consider the summation over the space of these lines $A \subset \mathbb{R}^2$, parallel to the condition that $\mu(t, \theta) \in \mathbb{R}^2$, with a line integral instead:

$$\mathscr{R}\mu(A) = \iint_A \mu(x, y)\, ds, \tag{9}$$

ds being the infinitesimal length along the line A. As a direct consequence of the lines producing peaks along the detector surface where they impinge, we may alternatively write Eq. 8 using the Dirac-delta function, which selectively chooses each line of interest over the detector region:

$$S(t, \theta) = \iint_{\mathbb{R}^2} \mu(x, y)\delta(t - x\cos\theta - y\sin\theta)\, dx\, dy. \tag{10}$$

The information that we wish to obtain, though, is not the Radon transform data, rather the attenuation density data μ, as the unique attenuation of each part of an object characterizes what material it is, according to condition 1. A first attempt at obtaining this data is by working in the reverse: by taking the Radon transform data and layering it over A by following back along the projection lines, and summing over all possible angles without double counting, we can reconstruct the object that was scanned. This method is known as back projection, given in Eq. 11 and shown in Fig. 2:

$$\mu_{BP}(x, y) = \mathscr{B}S(x, y) = \frac{1}{\pi}\int_0^{\pi} S(t, \theta)\, d\theta. \tag{11}$$

[5]That is, for constants a, b and functions f, g: $\mathscr{R}(af + bg) = a\mathscr{R}f + b\mathscr{R}g$ and $\mathscr{R}f(x, y) = \mathscr{R}f(-x, -y)$, respectively.

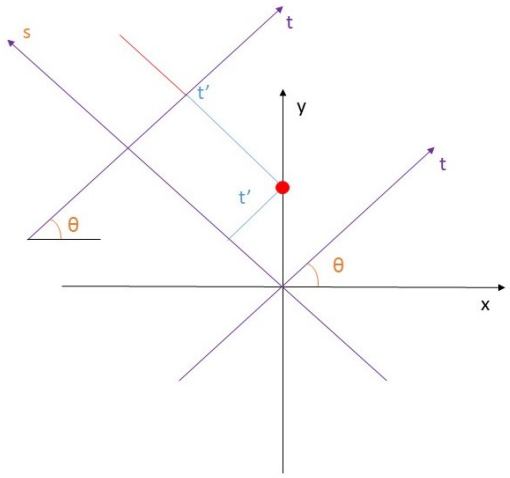

Figure 2: The back projection of a point source (red) into the $t - \theta$ coordinate system, from the xy coordinate system. The location t' of the spike resultant from the point source along a 1D detector is given by $t = r \sin\theta$, where r is the position of the point source along the y-axis. A projection of a full body source produces, roughly, a sine function.

Back projection alone, however, does not produce an intelligible reconstructed image. In practice, when we back project the object to reconstruct an image, what is unintentionally included are all other sources which interact with the object as well, producing a blurry image due to noise from primarily low-intensity sources. What must be done, then, is to cleave the noise from the back projected data, typically achieved using some kind of filter. The method of filtered back projection (FBP), one of the foremost reconstruction techniques, becomes clear: given a set of intensity data, we can back project it over various viewing angles while removing sources of noise via apt usage of filters. We can derive the inverse Radon transform and recover the attenuation density information:

$$\mu(x,y) = -\frac{1}{2\pi^2}\int_0^\pi \int_{\mathbb{R}} \frac{\partial S(t,\theta)}{\partial t}\frac{1}{t - x\cos\theta - y\sin\theta}\,dt\,d\theta. \tag{12}$$

Eq. 12 has a rather abstract form as given. Rewriting this equation with Fourier analysis, specifically through the usage of the Fourier transform, inverse Fourier transform, and the Fourier slice theorem, including the back projection operator defined in Eq. 11, we obtain[6]

$$\mu(x,y) = \frac{1}{2}\mathscr{B}[\mathscr{F}^{-1}(|T|\mathscr{F}S(t,\theta))](x,y). \tag{13}$$

[6]For a full discussion on the derivation of the inversion formula for the Radon transform, especially in dimensions greater than 2, refer to [44].

The process of FBP becomes clear: by taking the Fourier transform of the sinogram, you multiply the result by a filtering factor $|T|$ and take the inverse Fourier transform, then apply a back projection to obtain the attenuation data. We may also rewrite Eq. 12 using the property of convolution between the measured intensity data and a filter ϕ, which cleaves the low-intensity blurring information out while accentuating high-intensity contrasting features in the data and also has a Fourier transform exactly equal to the filtering factor. This is written as:

$$\mu(x, y) = \mathscr{B}(S * \phi) = \int_0^{\pi} S(t, \theta) * \phi(t)\, d\theta. \tag{14}$$

2.2 Alternate Reconstruction Methods

In the realm of DT, one of the earliest methods of image reconstruction was the shift-and-add method, in all ways equivalent to the aforementioned standard back projection method sans filtration. FBP was one of the first deblurring methods to account for the shift-and-add method's reduced contrast in images, another such method being matrix inversion tomosynthesis (MITS). MITS accounts for a local blurring matrix in individual tomosynthesis slices that, through Fourier and matrix inversion, can be subtracted from all other slices to heighten the contrast of anatomical regions of interest [17], [21]. Comparing the two, MITS has shown noted advantages over FBP with high-frequency content while FBP handles low-frequency data with greater accuracy than MITS [45]. In terms of application, FBP was certainly the standard method of reconstruction and deblurring in imaging due to it being a long-time practice that is comparatively easy to understand and implement. There have been attempts at combining MITS and FBP, appealing to the advantages of both methods while trying to minimize the faults of either, in what is called Gaussian frequency blending (GFB). By blending a low-pass and high-pass Gaussian filter, effectively mixing the methods of FBP and MITS respectively, into a weighted distribution, it is possible for improvements to identifying both high and low-frequency content in bodies while reducing noise [45].

At current, though, methods such as FBP, MITS, and GFB have been substituted for iterative reconstruction (IR) techniques with Siemens Healthineers introduction of the iterative reconstruction in image space, or IRIS, algorithm in 2009. Most IR algorithms obey a set of core principles: the algorithm starts with an image that is assumed to be equivalent to the actual bodily image being produced and is corrected to match the actual patient based on the difference between the assumed model's projection data and the actual projection data of the patient. As of current, IR is paving the way in reconstruction, current algorithms including GE Healthcare's adaptive statistical iterative reconstruction (ASIR-V), Philips Healthcare's iterative model reconstruction (IMR) and iDose^4, Siemens Healthineers advanced modeled iterative reconstruction (ADMIRE), and Canon Healthcare's forward projected model-based iterative reconstruction solution (FIRST) [11], [46].

3 Methods

> Do not read so much, look about you and think of what you see there.
>
> *Richard Feynman* [47]

3.1 Creating a Final Image

By utilization of any one of the methods discussed in Sec. 2.2, one can develop a collection of tomographic slice images, referred to as an image stack, that can be processed into a final image that contains the information of each individual slice. Reconstruction is not a perfect process, however. Given the necessity to develop images within a reasonably short time frame, a balance must be struck between developing images rapidly, with minimal information loss, with file sizes that are not too large, and are readily accessible to both human and software analysis. A wide variety of processing tools already exist which can produce 2D and even 3D final images, such as MATLAB's image processing toolbox and related DICOM-based commands, or ImageJ's image analysis features. The discussion henceforth will revolve around MATLAB code developed in the Zhou laboratories, originally written by Dr. Connor Puett for digital breast tomosynthesis and intraoral tomosynthesis, that has been modified to process chest tomography scans.[7] A description of how the code functions are what follows. The collection of images investigated came from a project utilizing a Carestream DRX chest radiograph against chest tomosynthesis scans from the same system performed on five different patients. System specifications are listed in Tables 1 and 2 for each patient's chest tomosynthesis and chest radiographs, respectively. Not included in the table is that the final synthetic images for the tomosynthesis scan, shown in Sec. 4, come from a combination of 116 total tomosynthesis slice images for each patient.

Definitions of the terms used in Tables 1 and 2 are given here, each of them important attributes taken from the patient's DICOM files:

1. Slice Thicnkess: A complete tomosynthesis scan of one person produces multiple images from the selected region at different layers. The spacing between these image layers is the slice thickness, with typical values on the order of millimeters.

2. kVp: The kilovoltage peak (kVp) is the greatest value produced from the X-ray device during an active exposure, that is, during an imaging event.

3. Exposure Time: The span of time under which an imaged volume is under X-ray radiation.

[7] There are original papers authored by Dr. Puett and members of the Zhou laboratories that describe the functioning and use of the code in practice, found in [48] and [49].

Table 1: Tomosynthesis Scan Data

	Slice Thicnkess	kVp	Exposure Time	Source Image Count	Exposure Time per Projection	S2D Distance	Tube Current	Exposure	Patient Orientation	Angle Span	Image Resolution	Viewable Image Size	Pixel Pitch
Patient 1	2.5 mm	80 kV	1445 ms	31	46 $\frac{\text{ms}}{\text{projection}}$	1.3261 m	5 mA	7 mAs	L\F	11.5905	1280 x 1536	355 x 427 mm	0.2780 x 0.2780 mm
Patient 2	2.5 mm	80 kV	1926 ms	31	62 $\frac{\text{ms}}{\text{projection}}$	1.2990 m	5 mA	10 mAs	L\F	11.8233	1280 x 1536	355 x 427 mm	0.2780 x 0.2780 mm
Patient 3	2.5 mm	80 kV	1711 ms	31	55 $\frac{\text{ms}}{\text{projection}}$	1.2678 m	5 mA	9 mAs	L\F	12.1234	1280 x 1536	355 x 427 mm	0.2780 x 0.2780 mm
Patient 4	2.5 mm	80 kV	1060 ms	31	34 $\frac{\text{ms}}{\text{projection}}$	1.2668 m	5 mA	5 mAs	L\F	12.1308	1280 x 1536	355 x 427 mm	0.2780 x 0.2780 mm
Patient 5	2.5 mm	80 kV	1079 ms	31	34 $\frac{\text{ms}}{\text{projection}}$	1.3056 m	5 mA	5 mAs	L\F	11.7403	1280 x 1536	355 x 427 mm	0.2780 x 0.2780 mm

Table 2: Radiograph Scan Data

	kVp	Exposure Time	Tube Current	Exposure	Patient Orientation	Area Dose Product	Focal Spot	Image Resolution	Viewable Image Size	Pixel Pitch
Patient 1	100 kV	7 ms	250 mA	2 mAs	L\F	1.5780 dGy $\cdot$ cm^2	1.2 mm	2520 x 3032	350 x 421 mm	0.1390 x 0.1390 mm
Patient 2	100 kV	6 ms	250 mA	2 mAs	L\F	1.3870 dGy $\cdot$ cm^2	1.2 mm	2520 x 3032	350 x 421 mm	0.1390 x 0.1390 mm
Patient 3	100 kV	6 ms	250 mA	2 mAs	L\F	1.3320 dGy $\cdot$ cm^2	1.2 mm	2520 x 3032	350 x 421 mm	0.1390 x 0.1390 mm
Patient 4	100 kV	6 ms	250 mA	2 mAs	L\F	1.1810 dGy $\cdot$ cm^2	1.2 mm	2520 x 3032	350 x 421 mm	0.1390 x 0.1390 mm
Patient 5	100 kV	6 ms	250 mA	2 mAs	L\F	1.2170 dGy $\cdot$ cm^2	1.2 mm	2520 x 3032	350 x 421 mm	0.1390 x 0.1390 mm

4. Source Image Count: The number of source images used in the development of the tomosynthetic image. Source images are images developed directly from the scan, they have a one-to-one pixel data relation. Derived images, on the other hand, are any other images included that have pixel values found by interpolating between the pixel data of the source images. The total number of images produced in a tomosynthesis scan is made up of both source and derived images.

5. Exposure Time per Projection: The amount of time it takes to scan over one of the source image regions. This is determined by dividing the exposure time by the number of source images.

6. S2D Distance: The distance between the X-ray source and the center of the detector region. This is also known as the source image receptor (SIR) distance.

7. Tube Current: The current passing through the X-ray source. The cathode of the X-ray tube is heated with a low-current voltage that, in the presence of a strong electric potential will have electrons break free from the cathode and attract strongly to a corresponding anode. The flow of the electrons between the cathode and anode is the tube current and is regulated by alternating the low-current voltage source.

8. Exposure: The amount of radiation produced over time from the system that is traveling to and through the patient.

9. Patient Orientation: The direction of orientation of the patient, given in the format of rows\columns. In this instance, the orientation of the patient is left\foot, or L\F. That is, the left side of the patient is on the right side of the image, and the feet of the patient are at the bottom of the image.

10. Angle Span: The angular span in degrees of rotation of the X-ray source during the image acquisition phase.

11. Area Dose Product: Specifically, this is the image and fluoroscopy area dose product. The X-ray dose that the patient was exposed to during the image acquisition including any fluoroscopic dosage used to aid image acquisition.

12. Focal Spot: The nominal focal spot size. The focal spot is the area from which the X-rays are generated in each instance along the outward panel of the source region. That is, the focal spot is the area of the anode from the X-ray tube that is illuminated by electrons jettisoned from the cathode.

13. Image Resolution: More specifically, this is the native image resolution for the patient scans. Given as the pixels per inch (PPI) for an image.

14. Viewable Image Size: Also known as the display size, the physical area spanned by the display of the image.

15. Pixel Pitch: The separation distance between any two consecutive pixels, given in both the horizontal and vertical directions. Typically, the smaller the pixel pitch, the higher the resolution of an image.

It is instructive to note the ways in which information from medical imaging scans is stored. Typically, an image from a medical scan is saved in the DICOM (Digital Imaging and Communications in Medicine) file format. DICOM files include both the image obtained from a medical scan, as well as important information about both the patient and the scanner device as well. This information is attached to each individual DICOM file as data sets listed as attributes to the image, embedded in such a way to prevent accidental separation of the identifying patient and scanner information from the image.

3.2 Image Initialization and Superficial Slices

Given a collection of tomographic slices, there are certain parameters that must be met in order for the images to be observed and our code to execute. We start by ensuring that each tomographic slice is cropped over the same region. If the tomographs include information out of the plane of interest, they must be removed before processing begins. Further, it is of importance that we understand how images are geometrically produced from the patient. Image slices acquired from chest tomosynthesis fill out a cone-like space: given the proportions of the body, as image slices pass from supracostal to intercostal, the spatial domain expands to fill a larger section of the body so as to include as much information as possible. Images, if not cropped before processing, can result in poor final image quality as shown in the image sequence of Fig. 3.

It is also a possibility that the superficial slices in the series can interfere with feature identification in the final result, as these images tend to include greater blur from a lack of focus over the region of interest. Evident in Figs. 3.(a) and (c) when compared to Fig. 3.(b), the focus on the chest is lacking at the supra- and infracostal slices when compared to the intercostal slice. To address this, we weigh the appropriate superficial slices such that their impact on the feature identification and segmentation are minimal, while still including important information from those slices. In particular, by down weighting the superficial slices in a segmented frequency stack, that is, a collection of images that can highlight unique characteristics that are displayed at certain frequencies, the impact of the blur from the superficial images is minimized.

3.3 Image Mask

It is equally important to assign to the image certain values which correspond to the outputted intensity of observable objects in the scanning region. We begin this process by generating an image mask for each set of data. The process of masking an image is what sets the background of the final image by assigning pixel values a weight relative to a unique threshold value. Values below the threshold are oftentimes set to zero (black), and values above that threshold

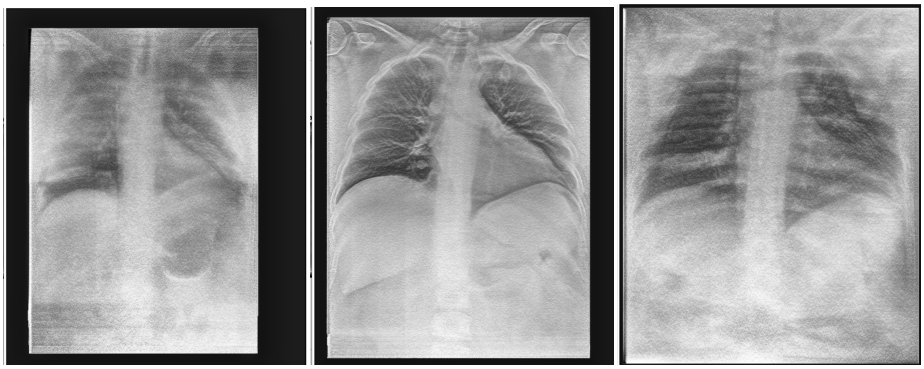

(a) Supracostal slice. (b) Intercostal slice. (c) Infracostal slice.

(d) Final image.

Figure 3: (a) - (c): Tomosynthesis slice images of patient 1 before cropping. Note the inclusion of the black space in the entire image space. (d): If the black space is not cropped and the images are not the same size, the resultant image will have a streaked layering artifact.

are displayed as they are, but weighted by their relative numerical separation from the threshold value. Typically, masking is achieved by either using a preexisting image as the mask or selecting multiple regions of interest (ROIs) that define the mask from each tomographic slice. As ROI-masking can be tailored to each image slice while constructing the mask profile and is generally more user-friendly and controllable, we adopt it as the main method of image mask generation for our project.

To determine the ROIs, one takes the average image projection and perform image segmentation to identify and group together pixels of the image which have similar elements. A popular method of image segmentation that we use here is k-means segmentation: by creating k-many homogeneous groups for pixels to be assigned to, with groups formed such that pixel elements are more similar to members of their assigned group than other groups, the pixels are

weighted to nearby clustered groups based on their distance from the center of the cluster and their similarity to the existing elements of the cluster. If the element is added to the new cluster, the center of the cluster changes until each cluster cannot add any more elements to itself or a pre-established runtime is exceeded. An example of this is shown in Fig. 4.

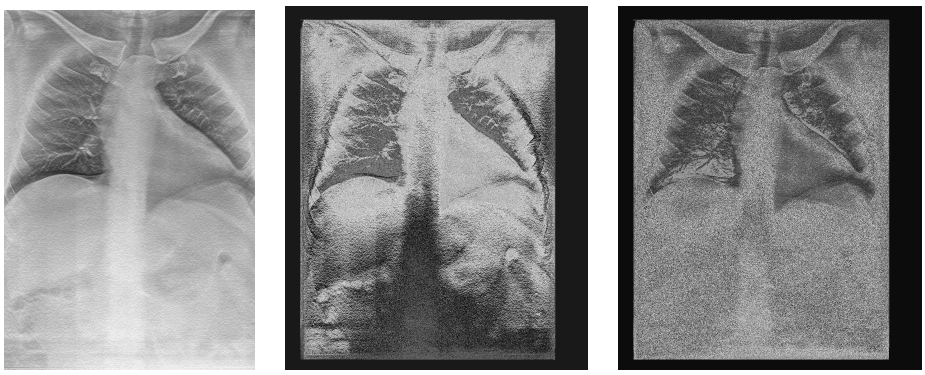

Figure 4: A k-means clustering of (left) one tomosynthesis slice from patient 1 of (middle) k = 10 and (right) k = 20. Note the inclusion of the lower left lungs in the right image as opposed to the middle image: with increasing k, the number of clusters and unique data points increase also. This clustering was performed using the open source IJ-Plugins Toolkit for ImageJ, accessible under [50].

As it is important to include as much information as possible within a tomographic slice, we can go further and obtain a soft mask of the image projection by weighting the intensity of pixels that surround an ROI but are not within a cluster and, instead of setting their value to the background, lower their intensity values proportional to the weight of the pixel amount if it were within the ROI. A hard mask on a k-means segmentation would result in all non-ROI pixels being set to the background without weighting. While soft masking can include more information that hard masking could set to be background values, soft masking inherently results in issues with contrast brightening: with a greater number of pixels, increasing the contrast becomes a proportionally more pronounced effect.

3.4 Segmentation and Identification

It is a natural consequence following the clustering of an image to perform segmentation upon it. The process of segmentation is what identifies pixel-level regions of interest from the background given distinctions between brightness, contrast, gray level, and texture between pixels [51]. Segmentation algorithms are unique to the whole body region that is being studied: a segmentation process tailored to the brain, for instance, would not perform well for a seg-

mentation of the breast due to a host of factors that account for partial volume effects, differing prominent artifacts, sensor and electronic noise, soft tissue gray level similarity, and the inhomogeneity of intensities in clusters [51], [52]. In the process of developing our image mask, we created k-many clusters that, during segmentation, are partitioned for higher analysis. K-means segmentation is a form of unsupervised learning, a process that does not necessarily require inputs or labeling from some external expert source.[8]

Blob detection and analysis typically follow pixel-based segmentation. Blob detection and analysis, or simply blob detection, is the differentiation of large-scale regions in an image by comparison of features such as orientation, area, and contrast. Notably, the differentiation of regions during blob detection is similar to the methods used during segmentation. This is not a surprising similarity: blob detection considers the multitude of blobs that construct an image, those being the pixel ROIs identified during segmentation, like pixels in segmentation, and processes them in a similar manner. A simple blob detection of the same tomographic slice from Fig. 4 is shown in Fig. 5.

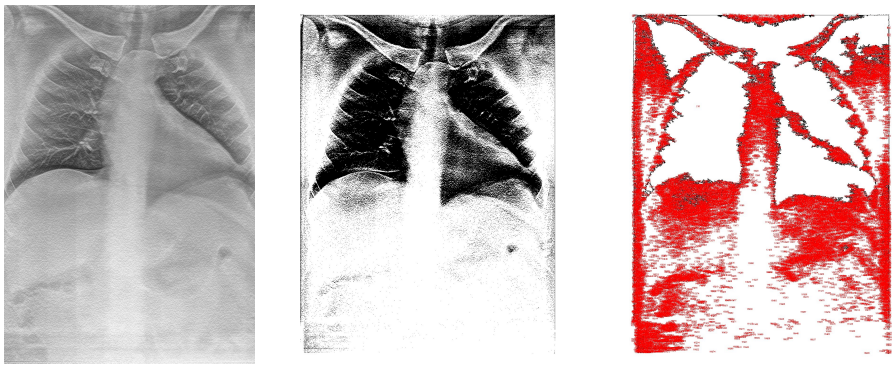

Figure 5: A simple blob detection from a single tomosynthesis slice of patient 1, with the (left) original image, (middle) the thresholded image, and (right) the image with detected blobs. A basic blob detection works as such: a base image is thresholded to identify objects in the image that is then outlined and filled, marked white, to clearly separate the blob from surrounding background regions, marked red, with black markers indicating the edges of the blob. This blob detection was performed using the Analyze Particles command prepackaged with ImageJ.

Of the many types of blob detectors, we use the maximally stable extremal regions, or MSER, method. A method with demonstrated power in detecting various regions of various sizes with a high degree of stability in reproducing the same regions under changes in view, scale, and light, the advantages that

[8]For this reason alone, the appeal to using k-means segmentation is large, especially with the rise of deep learning methods that can improve the performance of the method. Refer to [53] for more.

MSER offers outweighs many of the easier to implement, but less rigorous, blob detectors [54]. In application, an MSER detection method parses through image frequency stacks to select potential regions that, based on that region's averaged pixel information, total size, and shape are identified to be blobs. The uniqueness, and strength, of MSER is the criterion for accepting blobs: as the name would suggest, blobs that are selected demonstrate a high level of invariance under various transforms, such as contrast shifting, position transforms, and dilation, being "maximally stable".[9] Similar to segmentation, any blob detector tailored for one region of the body would perform poorly if used for another bodily region, as the determination of potential and actual blobs differs for the region of the body being considered.

3.5 Weighted Forward Projection and Recombination

Once blobs have been identified through blob detection, with the characteristics of each blob determined through segmentation, we turn our focus into enhancing the focus of our final image to emphasize unique ROIs and their immediate background while de-emphasizing surrounding objects such as tissue and bone. This can be achieved by creating a weighting function that weights the determined ROIs from each tomographic slice against the mask of each slice. Once the weighting function of the ROIs is developed, it is convolved against the image mask through the entire image stack and smoothed to correct for sharp weighting around the boundaries of ROIs and the edges of the image. When a weighting function is applied to an entire image stack in such a way, the process is known as a weighted forward projection, as the weighting starts with the initial image in the stack, updating with each subsequent tomographic slice in the depth of the image until the final image is weighted. Once the weighted forward projection is completed, the images in the stack can be recombined to produce the final synthetic image. Image recombination is typically achieved through a form of pyramid representation which aids in the identification of patterns in a produced image, determining properties unique to specific blobs, reducing noise in an image, and sharpening image features [56], [57]. Any class of bandpass pyramid generation is ideal as it allows for better distinctions between ROI pixel values per image structure. The Laplacian pyramid is a simple yet effective bandpass pyramid method, derived from the Gaussian pyramid. In a Gaussian pyramid method applied to an image stack, an original image is weighted down by applying a Gaussian blur and dilated down by half of its original size, as shown in Fig. 6. The Laplacian pyramid, on the other hand, takes images from a Gaussian pyramid and subtracts from them the preceding Gaussian pyramid image, properly scaled so sizes match, the difference being the Laplacian pyramid. Developing images as a Laplacian pyramid is particularly useful as the resulting pyramid is easily compressible, unlike Gaussian pyramid images, and can return the original image with few manipulations as it is an invertible image representation [57].

[9] For a more complete discussion of the stability of MSER-selected blobs, refer to [54] and [55].

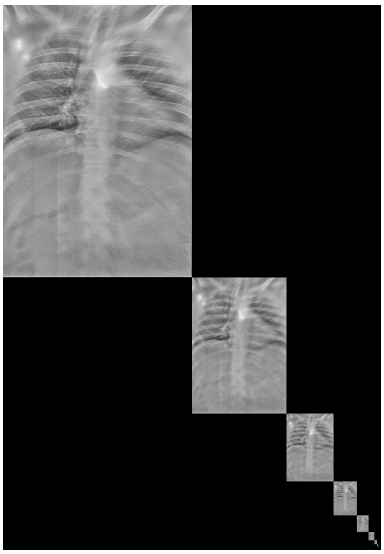

Figure 6: A Gaussian pyramid of the final synthetic image for patient 1, of order 9. The order of the pyramid starts with the top left image at zero, and with subsequent levels the prior ordered image undergoes a Gaussian blur and is subsampled to produce an image of halved resolution. This Gaussian pyramid was created using the Image Pyramid plugin for ImageJ, accessible under [58].

In the process of recombination, it is important to account for any potential differences in the backgrounds of each individual slice before the synthetic image is produced. This is handled by correcting the backgrounds of each image with an equalization process. In this case, we use histogram equalization, also known as windowing or gray level mapping, as the relevant intensity data for each slice has already been determined through the k-means segmentation process. With the full range of intensities for each image collected, histogram equalization enhances the contrast of regions with lower contrast that are near the background threshold by normalizing the blob regions which all possess a similar intensity to one another, that is, the collection of intensity values that are most prominent in the original image is adjusted down to enhance the contrast of the intensity values that are not as prominent.

The reason *why* it is called a synthetic image is now evident: a synthetic image is one that has undergone some computational manipulations before recombination to emphasize select features. The actual acquisition of the image, which is discussed in Sec. 2, does not determine if an image is a synthetic one or not, it is the processing of the image after the image acquisition that does. The total process outlined in these methods to obtain an image ready for projection and recombination, those being to initialize the image stack to unique parameters and perform a segmentation and blob identification on an image mask, shall henceforth be referred to as the PRIISM (to **P**roject and **R**ecombine, you **I**nitialize to **I**dentify and **S**egment the **M**ask) method.

4 Results and Analysis

> ...what we observe is not nature
> in itself, but nature exposed to
> our method of questioning.
>
> *Werner Heisenberg* [59]

The total stack synthetic tomosynthesis images for each investigated patient, including their chest radiographs, are shown in Figs. 7-11. Each of the chest radiographs was windowed using ImageJ's prepackaged window and leveling tool. There are a host of notable differences between the synthetic and radiographic images for each patient that I shall discuss the most noteworthy of.

As is evident for each of the synthetic images when compared to their radiograph counterparts, the bodily coverage is not as great in each synthetic image. As discussed in Sec. 3.2, the entire image stack for each patient was cropped around the first superficial image of the stack, that being the smallest, to avoid streaking. A way in which larger portions of the body can be included would be to instead produce a slab image. Slab images recombine only a portion of the image stack and, as a result, will always contain less image information than if the entire stack was recombined, but if done properly can highlight important features that would otherwise be overlooked and, in this case, include a larger area of the chest.

Looking particularly at Figs. 7, 8, and 10 note the large white spots in the normal synthetic image that are not found in the radiograph. These bright spots are areas with a correspondingly high-intensity and appear white, while areas with low-intensity values are darker in color. The intensity of these bright spots is enhanced with histogram equalization, so a balance must be struck between the intensity and size of the bright spots and the level to which the image is windowed. As an aid in determining what is an acceptable windowing level, the Hounsfield units (HU) are often used.[10] A scale which describes the radiodensity of materials with distilled water intentionally set as the zero point, the Hounsfield units are useful for characterizing anatomical structures which contain water and can easily be separated from air, making it self-evident why they would well-describe human anatomy. Setting a window level to the approximate HU of an anatomical structure highlights its anatomy and internal components.

Each of the synthetic images also demonstrates a greater presence of rib bones than their radiograph counterparts. The brightening of the bone material in these images is a consequence of the limited angular span of tomosynthesis. As aforementioned, each of the tomosynthesis image stacks spans the range from being supracostal to infracostal and, consequently, will include the bones wrapping over, along, and behind the internal organs of the chest with short angular movement. A heavy-handed solution to this problem can be found by

[10] Named after the very same Sir Godfrey Hounsfield who championed the advent of CT technology.

slabbing the image stack over only the intercostal region if the structures of study are the internal organs rather than the bones, but it is not a perfect solution and, as it turns out, removing the ribs from chest tomosynthesis scans is a particularly tricky and difficult task [60]. The code also includes additional aspects not mentioned in Sec. 3, those being processes that enhance the presence of particular features in the final synthetic image. Enhancement features are optional for producing the final synthetic image but can visually highlight important features above others. Here, the included enhancement feature impacts the intensity histogram during histogram equalization to make high-intensity, or bright, features more prominent. Since the HU of the bone is significantly greater than air, water, and internal organs, any bone material will already be bright compared to any internal structures and will be impacted by the enhancement. A simple solution would be to remove the bright enhancement feature altogether, correcting for both the bone presence and many of the bright spots.

Each of the synthetic images shows a notable grayscale color difference from their chest radiographs, the result of the intensity histograms being different from one another. In the production of the synthetic image, the multitude of histogram modifications that were done has impacted the intensity values. It is an issue of the synthetic and radiograph intensity histograms being offset from one another and the histograms not spanning the same width, which results in discoloration. There is not an easily implementable direct solution to this issue, but there are tests that exist to determine if the qualities of the produced images are comparable and can be used interchangeably. An evaluation of the receiver operating characteristic curve (ROC curve), for instance, could confirm the level of agreement in both the synthetic and radiograph images for identifying structures in both such as organ location, organ type, and others.[11]

Of critical importance in medical imaging is evaluating the presence of any artifacts in an image. An artifact is a general term that encompasses any one of the many ways structures of the body can be misinterpreted due to the way in which an image was captured, whether it be the process of acquisition itself, complications with unaccounted internal body structures, or some other factor. Each of the synthetic images has a somewhat subtle blur over the entire image that appear as streaks over the entire image, while the radiographs have no such artifact. It is only truly evident that this is an involuntary motion artifact present in each patient when we refer to the scan times in Tables 1 and 2. When comparing the exposure times for the tomosynthesis scans to the corresponding radiograph exposure times, there is an immediately notable difference: most of the tomosynthesis scans are nearly 200 times longer than the corresponding chest radiograph. While all of the radiographs span the order of a few milliseconds, all of the final synthetic images are produced on the order of 1000 to nearly 2000 milliseconds. A normal human heart can, for instance, beat once or twice within the order of a second. Including all other involuntary organ movements within the entire chest cavity, the amount of movement that takes place between the

[11] A ROC curve evaluation ranks, in this case, the ability of an image to produce true positive results against its false positive rate. The greater the probability of detection is against its probability of false alarm, the better the image is for the purposes of evaluation.

entire tomosynthesis scan and the radiograph are vastly different. Note that the final synthetic tomosynthesis image is a collection of multiple images collected over the entire exposure time, while the radiograph image is a single image. To discuss the time between slices when compared to the single radiograph, it is better to use the exposure time per projection value, than the total exposure time. Potential solutions would be to reduce the exposure times during the image acquisition phase or to slab the imaging region. Since an image slab only considers a portion of the total images used, the exposure time needed to acquire the slab will always be less than the total exposure time and, consequently, will have reduced involuntary movement. Given the exposure time per projection and the scale of the imaging region, however, the effects of slabbing are negligible in decreasing the overall involuntary motion blur, instead notably reducing the in-plane spatial resolution when compared to the total stack synthetic image.

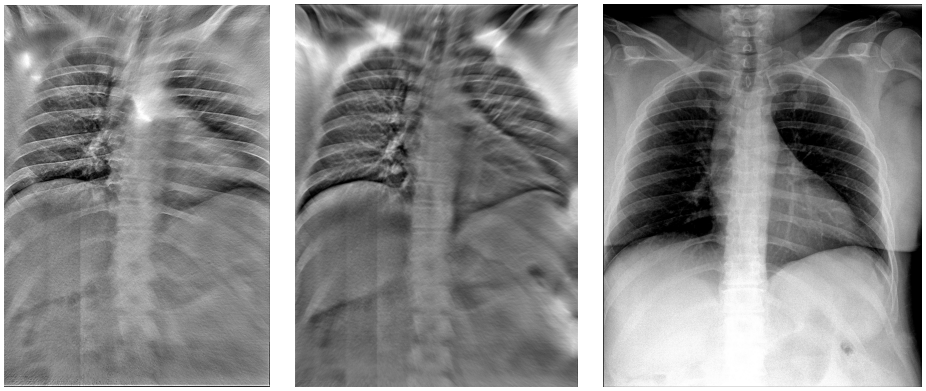

Figure 7: (left) Synthetic, (middle) slabbed synthetic, and (right) radiograph images for patient 1. The slabbed synthetic image spans the region of the lungs with a de-emphasis of the supracostal and infracostal ribs.

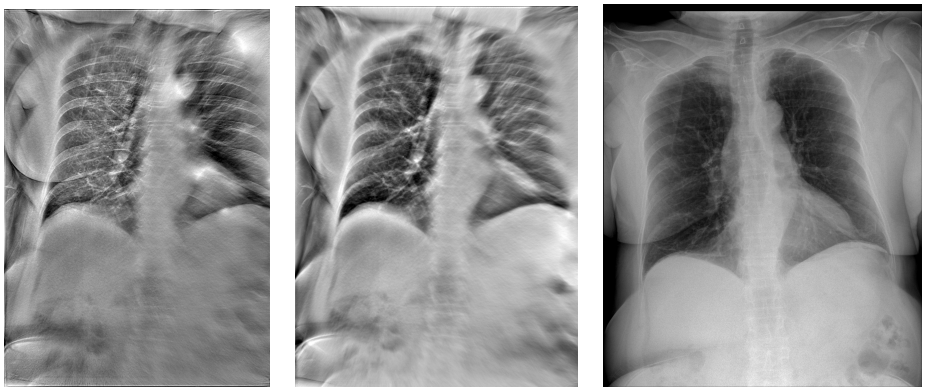

Figure 8: (left) Synthetic, (middle) slabbed synthetic, and (right) radiograph images for patient 2. The slabbed synthetic image spans the region of the lungs with a de-emphasis of the supracostal and infracostal ribs.

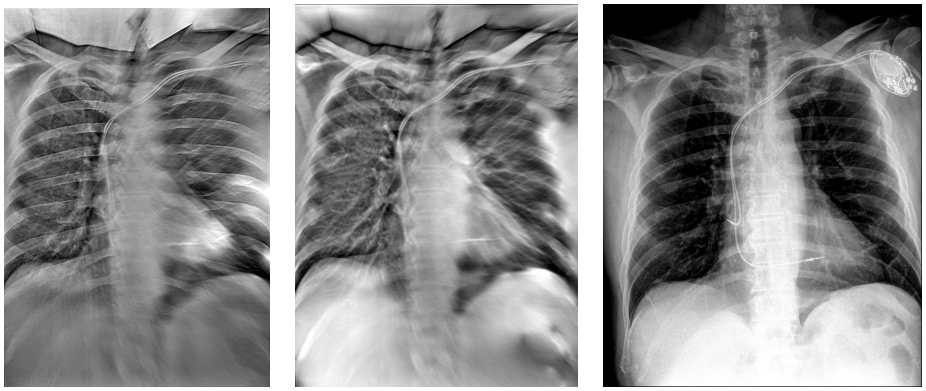

Figure 9: (left) Synthetic, (middle) slabbed synthetic, and (right) radiograph images for patient 3. The slabbed synthetic image spans the region of the lungs with a de-emphasis of the supracostal and infracostal ribs.

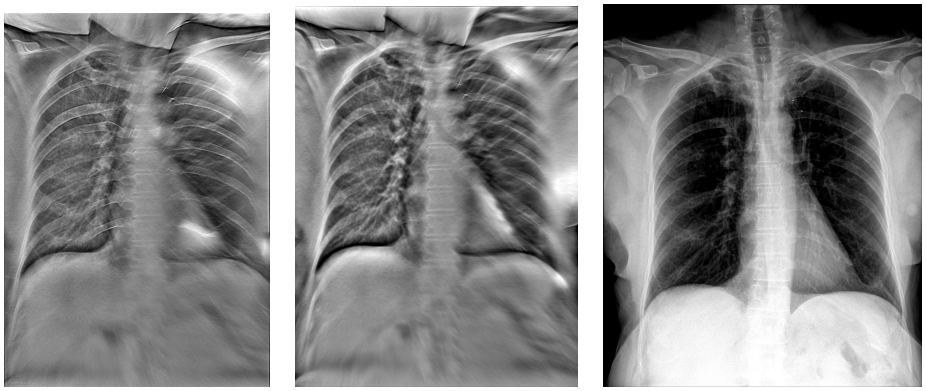

Figure 10: (left) Synthetic, (middle) slabbed synthetic, and (right) radiograph images for patient 4. The slabbed synthetic image spans the region of the lungs with a de-emphasis of the supracostal and infracostal ribs.

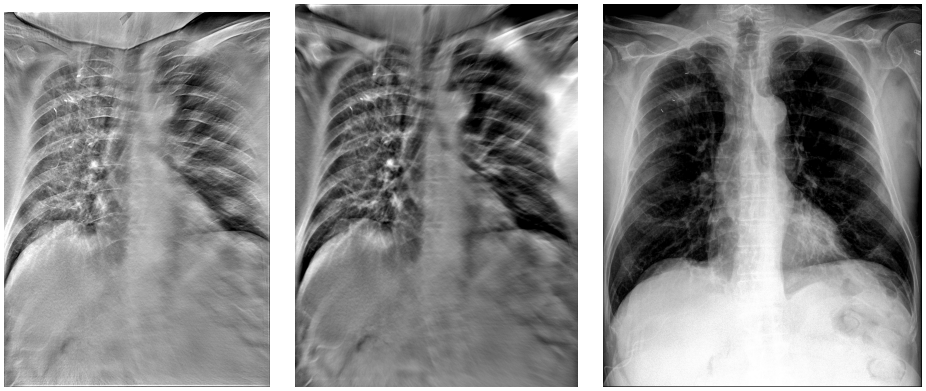

Figure 11: (left) Synthetic, (middle) slabbed synthetic, and (right) radiograph images for patient 5. The slabbed synthetic image spans the region of the lungs with a de-emphasis of the supracostal and infracostal ribs.

5 Discussion and Conclusion

> But still try, for who knows what is possible...
>
> *Michael Faraday* [61]

5.1 Discussion of Results

The PRIISM method has shown potential by producing images that share a definite likeness to their radiograph counterparts. The PRIISM method, though, is not perfect and there are many ways in which it can be improved.

Image initialization can be improved by providing more robustness to the MATLAB code to handle varying types of image stacks. Of primary interest would be providing the means to check over neighboring images in a stack to predetermine if image cropping is a necessity, saving time by eliminating the need to examine image stacks and manually crop them, along with potential information loss via image file type conversion for processing in ImageJ. The production of the image mask, also, can be updated by improving the clustering process. Selecting the optimal number of clusters k that sufficiently characterize the body while not impacting the runtime of the clustering process, with the addition of ineffectual information, can be achieved by analyzing the intra-cluster variation for various values of k. This method of determining an optimal value for k is known as the elbow method as plotting the within-cluster sum of squares (WCSS) against k typically appears as an exponential decay, and the optimal k value is found in-between the initially sharp decreasing behavior and the long-term slowly decreasing behavior of the plot. The optimal k is the "elbow" of the graph, which separates the two distinct "arms" from one another. Further, k-means segmentation is liable to fall victim to the random initialization trap where, if the centroid of a determined cluster is randomly initialized, then different WCSS vs. k graphs will be produced for each test. This can impact the choice of k and, consequently, result in suboptimal clustering by the elbow method. A solution to this problem was found in [62] with the so-called k-means ++ segmentation, and implementing its methodology would be useful in circumventing poor choices of k and improving the location of the centers for ROIs. In the projection phase, a variety of different synthetic images can be developed to highlight the presence, or lack, of a particular feature with highly characteristic, distinguishable attributes. Of particular importance in chest imaging is the screening of lung nodules and lesions, along with mycobacterial infections. Generating separate synthetic images that are weighted specifically to emphasize these unique objects and harmful substances can significantly aid in the process of identifying them in the first place.

Of the image quality for the synthetic images, while the produced images are not perfect nor one-to-one with their radiographic counterparts, most of the notable issues with the image quality are not only expected but can also

be reduced by more advanced computational means. The most prevalent issue across each of the tomosynthetic image stacks is the blur due to involuntary bodily motion over the long exposure time during the image acquisition phase. It will be worth investigating additional patient data sets with reduced exposure times per projection to definitively conclude if reducing the exposure time will reduce the motion blur with the PRIISM algorithm, or highlight if the blur is the result of another unaccounted for issue nested within the code itself.

The study of these patient data sets is ongoing. Current studies and future projects are aimed at simulating tomosynthetic images at various angular coverages with the goal to cover a 3-dimensional space. In order to do so, a chest phantom needs to be created that can undergo a modeled x-ray projection which can then be reconstructed in a similar manner to the process above. The power needed to generate such models is high and requires laboratory-grade computer processors to complete. Generation of the chest phantom model, though, is not nearly as intensive. The 4D extended cardiac-torso (XCAT) phantom software is a command-line application where users can produce phantom models with an extended collection of modifiable parameters to fine-tune any phantom to set conditions [63]. With XCAT chest phantom models developed, the phantom would undergo an X-ray projection scan and the images from that would be reconstructed into a final 3D synthetic image. The ASTRA toolbox is an open-source MATLAB and Python toolbox for 2D and 3D tomography and can generate a 3D model from a given set of phantom data [64]–[66]. With the ASTRA toolbox, it is possible to model an X-ray projection and recombine the produced images in one execution of the associated code. With the easing of restrictions to laboratory access due to COVID-19, first-pass multi-angle coverage chest models are predicted to be completed by late April of 2022.

5.2 Conclusion

As recently as February of 2022, studies have been and are being carried out to investigate the effectiveness of, and potential improvements to, digital tomosynthesis technology, including modern research in the fields of DCT and DBT [60], [67]–[70]. The field of digital tomosynthesis is growing and retains a vast potential in aiding the medical imaging community by highlighting important features otherwise overlooked in the standard imaging modalities of today including chest radiography, breast mammography, and others. Understanding the process by which synthetic images are produced in this growing field is of critical importance in appreciating the benefits of, and limitations associated with, DT technology. PRIISM is both an easily understood and readily implementable method and serves as a standing review of the important factors which govern synthetic image production. Future iterations of this model will confirm its viability as a tool for clinical use, as a comparison tool, and potential ally to modern chest radiography.

6 References

[1] P. Dirac, "The scientific work of georges lemaitre," *Commentarii (Pontifical Academy of Sciences)*, vol. 2, no. 11, pp. 1–18, 1968.

[2] U. of Washington Department of Radiology. (2021). "Featured history: Wilhelm röntgen," [Online]. Available: https://rad.washington.edu/blog/featured-history-wilhelm-rontgen/.

[3] golanlevin. (2015). "First medical x-ray by wilhelm röntgen of his wife anna bertha ludwig's hand - 18951222," [Online]. Available: https://live.staticflickr.com/279/18673872934_bc56a30a87_m.jpg. License: CC BY 2.0.

[4] K. Sansare, V. Khanna, and F. Karjodkar, "Early victims of x-rays: A tribute and current perception," *Dentomaxillofacial Radiology*, vol. 40, pp. 123–125, 2011. DOI: 10.1259/dmfr/73488299.

[5] R. Sapir, M. Patlas, S. D. Strano, I. Hadas-Halpern, and N. I. Cherny, "Does mammography hurt?" *Journal of Pain and Symptom Management*, vol. 25, no. 1, pp. 53–63, 2003. DOI: 10.1016/S0885-3924(02)00598-5.

[6] J. E. de Groot, M. J. Broeders, C. A. Grimbergen, and G. J. den Heeten, "Pain-preventing strategies in mammography: An observational study of simultaneously recorded pain and breast mechanics throughout the entire breast compression cycle," *BMC Women's Health*, vol. 15, no. 26, 2015. DOI: 10.1186/s12905-015-0185-2.

[7] E. C. Lin, "Radiation risk from medical imaging," *Mayo Clin Proc*, vol. 85, no. 12, pp. 1142–1146, 2010. DOI: 10.4065/mcp.2010.0260.

[8] L. Shi and S. Tashiro, "Estimation of the effects of medical diagnostic radiation exposure based on dna damage," *Journal of Radiation Research*, vol. 59, no. S2, pp. ii121–ii129, 2018. DOI: 10.1093/jrr/rry006.

[9] J. Knott, L. Varangu, K. Waddington, T. Easty, and S. Shi, "Medical imaging equipment study: Assessing opportunities to reduce energy consumption in the health care sector," Canadian Coalition for Green Health Care, 2017.

[10] T. Heye, R. Knoerl, T. Wehrle, D. Mangold, A. Cerminara, M. Loser, M. Plumeyer, M. Degen, R. Lüthy, D. Brodbeck, and E. Merkle, "The energy consumption of radiology: Energy- and cost-saving opportunities for ct and mri operation," *Radiology*, vol. 295, no. 3, pp. 593–605, 2020. DOI: 10.1148/radiol.2020192084.

[11] S. Ravishankar, J. C. Ye, and J. A. Fessler, "Image reconstruction: From sparsity to data-adaptive methods and machine learning," *Proc IEEE Inst Electr Electron Eng*, vol. 108, no. 1, pp. 86–109, 2020. DOI: 10.1109/JPROC.2019.2936204.

[12] V. Antun, F. Renna, C. Poon, B. Adcock, and A. C. Hansen, "On instabilities of deep learning in image reconstruction and the potential costs of ai," *Proceedings of the National Academy of Sciences*, vol. 117, no. 48, pp. 30 088–30 095, 2020, ISSN: 0027-8424. DOI: 10.1073/pnas.1907377117. eprint: https://www.pnas.org/content/117/48/30088.full.pdf. [Online]. Available: https://www.pnas.org/content/117/48/30088.

[13] N. Tirada, G. Li, D. Dreizin, L. Robinson, G. Khorjekar, S. Dromi, and T. Ernst, "Digital breast tomosynthesis: Physics, artifacts, and quality control considerations," *RadioGraphics*, vol. 39, no. 2, pp. 413–426, 2019, PMID: 30768362. DOI: 10.1148/rg.2019180046. eprint: https://doi.org/10.1148/rg.2019180046. [Online]. Available: https://doi.org/10.1148/rg.2019180046.

[14] S. Pacifici and A. Murphy. (2021). "Digital breast tomosynthesis," [Online]. Available: https://radiopaedia.org/articles/15235.

[15] A. S. Ha, A. Y. Lee, D. S. Hippe, S.-H. S. Chou, and F. S. Chew, "Digital tomosynthesis to evaluate fracture healing: Prospective comparison with radiography and ct," *American Journal of Roentgenology*, vol. 205, no. 1, pp. 136–141, 2015, PMID: 26102392. DOI: 10.2214/AJR.14.13833. eprint: https://doi.org/10.2214/AJR.14.13833. [Online]. Available: https://doi.org/10.2214/AJR.14.13833.

[16] I. Sechopoulos, "A review of breast tomosynthesis. part i. the image acquisition process," *Medical Physics*, vol. 40, no. 1, p. 014 301, 2013. DOI: https://doi.org/10.1118/1.4770279. eprint: https://aapm.onlinelibrary.wiley.com/doi/pdf/10.1118/1.4770279. [Online]. Available: https://aapm.onlinelibrary.wiley.com/doi/abs/10.1118/1.4770279.

[17] A. Ferrari, L. Bertolaccini, P. Solli, P. O. D. Salvia, and D. Scaradozzi, "Digital chest tomosynthesis: The 2017 updated review of an emerging application," *Annals of Translational Medicine*, vol. 6, no. 5, 2017, ISSN: 2305-5847. [Online]. Available: https://atm.amegroups.com/article/view/16290.

[18] T. Gomi, M. Nakajima, H. Fujiwara, T. Takeda, K. Saito, T. Umeda, and K. Sakaguchi, "Comparison between chest digital tomosynthesis and ct as a screening method to detect artificial pulmonary nodules: A phantom study," *The British Journal of Radiology*, vol. 85, e622–e629, 2012. DOI: 10.1259/bjr/12643098.

[19] J. Dobbins 3rd and H. McAdams, "Chest tomosynthesis: Technical principles and clinical update," *Eur J Radiol*, vol. 72, no. 2, pp. 244–251, 2009. DOI: 10.1016/j.ejrad.2009.05.054.

[20] V. B. Kalra, X. Wu, B. M. Haas, H. P. Forman, and L. E. Philpotts, "Cost-effectiveness of tomosynthesis in annual screening mammography," *American Journal of Roentgenology*, vol. 207, no. 5, pp. 1152–1155, 2016, PMID: 27547861. DOI: 10.2214/AJR.15.14487. eprint: https://doi.

org/10.2214/AJR.15.14487. [Online]. Available: https://doi.org/10.2214/AJR.15.14487.

[21] J. T. Dobbins and D. J. Godfrey, "Digital x-ray tomosynthesis: Current state of the art and clinical potential," *Physics in Medicine and Biology*, vol. 48, no. 19, R65–R106, Sep. 2003. DOI: 10.1088/0031-9155/48/19/r01. [Online]. Available: https://doi.org/10.1088/0031-9155/48/19/r01.

[22] V. Backlund, "Simultaneous telefilm planigraphy," *Acta Radiologica*, vol. 41, no. 5, pp. 425–434, 1954. DOI: 10.3109/00016925409175866.

[23] D. Wheeler and E. W. Spencer, "Simplified planigraphy," *Radiology*, vol. 34, no. 4, pp. 499–502, 1940. DOI: 10.1148/34.4.499. eprint: https://doi.org/10.1148/34.4.499. [Online]. Available: https://doi.org/10.1148/34.4.499.

[24] J. B. Garrison, D. G. Grant, W. H. Guier, and R. J. Johns, "Three dimensional roentgenography," *American Journal of Roentgenology*, vol. 105, no. 4, pp. 903–908, 1969. DOI: 10.2214/ajr.105.4.903. eprint: https://doi.org/10.2214/ajr.105.4.903. [Online]. Available: https://doi.org/10.2214/ajr.105.4.903.

[25] D. G. Grant, "Tomosynthesis: A three-dimensional radiographic imaging technique," *IEEE Transactions on Biomedical Engineering*, vol. BME-19, no. 1, pp. 20–28, 1972. DOI: 10.1109/TBME.1972.324154.

[26] E. Klotz and H. Weiss, "Three-dimensional coded aperture imaging using nonredundant point distributions," *Optics Communications*, vol. 11, no. 4, pp. 368–372, 1974, ISSN: 0030-4018. DOI: https://doi.org/10.1016/0030-4018(74)90238-7. [Online]. Available: https://www.sciencedirect.com/science/article/pii/0030401874902387.

[27] G. Stiel, L. Stiel, E. Klotz, and C. Nienaber, "Digital flashing tomosynthesis: A promising technique for angiocardiographic screening," *IEEE Transactions on Medical Imaging*, vol. 12, no. 2, pp. 314–321, 1993. DOI: 10.1109/42.232261.

[28] G. M. Stevens, R. Fahrig, and N. J. Pelc, "Filtered backprojection for modifying the impulse response of circular tomosynthesis," *Medical Physics*, vol. 28, no. 3, pp. 372–380, 2001. DOI: https://doi.org/10.1118/1.1350588. eprint: https://aapm.onlinelibrary.wiley.com/doi/pdf/10.1118/1.1350588. [Online]. Available: https://aapm.onlinelibrary.wiley.com/doi/abs/10.1118/1.1350588.

[29] E. F. Conant, S. P. Zuckerman, E. S. McDonald, S. P. Weinstein, K. E. Korhonen, J. A. Birnbaum, J. D. Tobey, M. D. Schnall, and R. A. Hubbard, "Five consecutive years of screening with digital breast tomosynthesis: Outcomes by screening year and round," *Radiology*, vol. 295, no. 2, pp. 285–293, 2020, PMID: 32154771. DOI: 10.1148/radiol.2020191751. eprint: https://doi.org/10.1148/radiol.2020191751. [Online]. Available: https://doi.org/10.1148/radiol.2020191751.

[30] C. Puett, C. Inscoe, A. Hartman, J. Calliste, D. K. Franceschi, J. Lu, O. Zhou, and Y. Z. Lee, "An update on carbon nanotube-enabled x-ray sources for biomedical imaging," *WIREs Nanomedicine and Nanobiotechnology*, vol. 10, no. 1, e1475, 2018. DOI: https://doi.org/10.1002/wnan.1475. eprint: https://wires.onlinelibrary.wiley.com/doi/pdf/10.1002/wnan.1475. [Online]. Available: https://wires.onlinelibrary.wiley.com/doi/abs/10.1002/wnan.1475.

[31] C. R. Inscoe, C. Puett, A. J. Billingsley, O. Zhou, J. Lu, and Y. Z. Lee, "Evaluation of patient-specific scatter-corrected digital chest tomosynthesis," in *Medical Imaging 2020: Physics of Medical Imaging*, G.-H. Chen and H. Bosmans, Eds., International Society for Optics and Photonics, vol. 11312, SPIE, 2020, pp. 506–515. DOI: 10.1117/12.2549316. [Online]. Available: https://doi.org/10.1117/12.2549316.

[32] E. T. Gunnell, D. K. Franceschi, C. R. Inscoe, A. Hartman, J. L. Goralski, A. Ceppe, B. Handly, C. Sams, L. A. Fordham, J. Lu, O. Zhou, and Y. Z. Lee, "Initial clinical evaluation of stationary digital chest tomosynthesis in adult patients with cystic fibrosis," *Eur Radiol*, vol. 29, no. 4, pp. 1665–1673, 2019. DOI: 10.1007/s00330-018-5703-9.

[33] M. A. Al-antar, C.-H. Hua, J. Bang, and S. Lee, "Fast deep learning computer-aided diagnosis of covid-19 based on digital chest x-ray images," *Applied Intelligence*, vol. 51, pp. 2890–2907, 2021. DOI: 10.1007/s10489-020-02076-6.

[34] M. Alhasan and M. Hasaneen, "Digital imaging, technologies and artificial intelligence applications during covid-19 pandemic," *Computerized Medical Imaging and Graphics*, vol. 91, pp. 1–22, 2021. DOI: 10.1016/j.compmedimag.2021.101933.

[35] J. W. von Goethe, "Faust. part 1," in. The Harvard Classics, 1808.

[36] J. Radon, "On the determination of functions from their integral values along certain manifolds," *IEEE Transactions on Medical Imaging*, vol. 5, no. 4, pp. 170–176, 1986. DOI: 10.1109/TMI.1986.4307775.

[37] J. Beatty, "The radon transform and the mathematics of medical imaging," Colby College, 2012, *Honors Theses*. Paper 646.

[38] J. B. III, "The radon transform," Harvard, 2020.

[39] P. A. Toft, "The radon transform - theory and implementation," Technical University of Denmark, 1996, Ph.D. Thesis.

[40] J. Hubbell and S. Seltzer. (1995). "Tables of x-ray mass attenuation coefficients and mass energy-absorption coefficients 1 kev to 20 mev for elements z = 1 to 92 and 48 additional substances of dosimetric interest," [Online]. Available: http://physics.nist.gov/PhysRefData/XrayMassCoef/cover.html.

[41] I. S. U. C. for Nondestructive Evaluation. (2022). "Transmitted intensity and linear attenuation coefficient," [Online]. Available: https://www.nde-ed.org/Physics/X-Ray/attenuationCoef.xhtml.

[42] F. Priamo and A. Murphy. (2021). "Linear attenuation coefficient," [Online]. Available: https://radiopaedia.org/articles/31918.

[43] J. H. Lambert and D. L. DiLaura, "Photometry, or, on the measure and gradations of light, colors, and shade," in. Illuminating Engineering Society of North America, 2001, Originally published in 1760.

[44] S. Heglgason, "Radon transform," in, Second. Birkhäuser Boston, 1999.

[45] Y. Chen, J. Y. Lo, J. A. Baker, and J. T. D. III, "Gaussian frequency blending algorithm with matrix inversion tomosynthesis (mits) and filtered back projection (fbp) for better digital breast tomosynthesis reconstruction," in *Proc. SPIE 6142*, vol. 6142, 2006, pp. 122–130. DOI: 10.1117/12.652264.

[46] M. J. Willemink and P. B. Noël, "The evolution of image reconstruction for ct—from filtered back projection to artificial intelligence," *Eur Radiol*, vol. 29, pp. 2185–2195, 2019.

[47] R. P. Feynman, "Perfectly reasonable deviations from the beaten track," in. Basic Books, 2005, Letter to Ashok Arora (January 4, 1967).

[48] C. Puett, C. Inscoe, J. Lu, Y. L. M.D., and O. Zhou, "Generating synthetic mammograms for stationary 3D mammography," in *Medical Imaging 2019: Physics of Medical Imaging*, T. G. Schmidt, G.-H. Chen, and H. Bosmans, Eds., International Society for Optics and Photonics, vol. 10948, SPIE, 2019, pp. 27–37. [Online]. Available: https://doi.org/10.1117/12.2513017.

[49] C. Puett, C. R. Inscoe, R. L. Hilton, M. W. Regan Anderson, L. Perrone, S. Puett, L. R. Gaalaas, E. Platin, J. Lu, and O. Zhou, "Applying synthetic radiography to intraoral tomosynthesis: A step towards achieving 3d imaging in the dental clinic," *Dentomaxillofacial Radiology*, vol. 50, no. 2, p. 20 200 159, 2021, PMID: 32666823. DOI: 10.1259/dmfr.20200159. eprint: https://doi.org/10.1259/dmfr.20200159. [Online]. Available: https://doi.org/10.1259/dmfr.20200159.

[50] J. Sacha. (2021). "Ij-plugins toolkit," [Online]. Available: https://github.com/ij-plugins/ijp-toolkit/wiki.

[51] N. Sharma and L. M. Aggarwal, "Automated medical image segmentation techniques," *Journal of Medical Physics*, vol. 35, no. 1, pp. 3–14, 2010. DOI: 10.4103/0971-6203.58777.

[52] D. Withey and Z. Koles, "Three generations of medical image segmentation: Methods and available software," *International Journal of Bioelectromagnetism*, vol. 9, no. 2, pp. 67–68, 2007.

[53] R. Tanaka, S. Nozaki, F. Goshima, and J. Shiraishi, "Deep learning versus the human visual system for detecting motion blur in radiography," *Journal of Medical Imaging*, vol. 9, no. 1, pp. 1–9, 2022.

[54] K. Mikolajczyk, T. Tuytelaars, C. Schmid, A. Zisserman, T. Kadir, and L. Van Gool, "A comparison of affine region detectors," *International Journal of Computer Vision*, vol. 65, no. 1 – 2, pp. 43–72, 2005. DOI: 10.1007/s11263-005-3848-x.

[55] K. T. M. Han and B. Uyyanonvara, "A survey of blob detection algorithms for biomedical images," in *2016 7th International Conference of Information and Communication Technology for Embedded Systems (IC-ICTES)*, 2016, pp. 57–60. DOI: 10.1109/ICTEmSys.2016.7467122.

[56] E. Adelson, C. Anderson, J. Bergen, P. Burt, and J. Ogden, "Pyramid methods in image processing," *RCA Engineer*, vol. 29, no. 6, pp. 33–41, 1984.

[57] E. L. Denton, S. Chintala, A. Szlam, and R. Fergus, "Deep generative image models using a laplacian pyramid of adversarial networks," *CoRR*, vol. abs/1506.05751, 2015. arXiv: 1506.05751. [Online]. Available: http://arxiv.org/abs/1506.05751.

[58] D. Prodanov. (2012). "Image pyramid," [Online]. Available: https://imagej.nih.gov/ij/plugins/pyramid/index.html.

[59] W. Heisenberg, "Physics and philosophy: The revolution in modern science," in. Penguin Classics, 2000, Originally published in 1958.

[60] Y. Sun, Q. Yao, Y. Lyu, J. Wang, Y. Xiao, H. Liao, and S. K. Zhou, "Rib suppression in digital chest tomosynthesis," vol. abs/2203.02772, 2022. [Online]. Available: https://arxiv.org/abs/2203.02772.

[61] H. B. Jones, Ed., *The Life and Letters of Faraday*. Cambridge Library Collection, 1870, vol. 2.

[62] D. Arthur and S. Vassilvitskii, "K-means++: The advantages of careful seeding," in *Proceedings of the eighteenth annual ACM-SIAM symposium on Discrete algorithms*, Society for Industrial and Applied Mathematics, 2007, pp. 1027–1035.

[63] W. Segars and B. Tsui. (). "4d extended cardiac-torso (xcat) phantom version 2.0," [Online]. Available: https://otc.duke.edu/technologies/4d-extended-cardiac-torso-xcat-phantom-version-2-0/.

[64] W. van Aarle, W. J. Palenstijn, J. Cant, E. Janssens, F. Bleichrodt, A. Dabravolski, J. D. Beenhouwer, K. J. Batenburg, and J. Sijbers, "Fast and flexible x-ray tomography using the astra toolbox," *Opt. Express*, vol. 24, pp. 25 129–25 147, 2016.

[65] W. van Aarle, W. J. Palenstijn, J. D. Beenhouwer, T. Altantzis, S. Bals, K. J. Batenburg, and J. Sijbers, "The astra toolbox: A platform for advanced algorithm development in electron tomography," *Ultramicroscopy*, vol. 157, 2015.

[66] W. J. Palenstijn, K. J. Batenburg, and J. Sijbers, "Performance improvements for iterative electron tomography reconstruction using graphics processing units (gpus)," *Journal of Structural Biology*, vol. 176, 2010.

[67] A. C. Burks, J. Akulian, C. R. MacRosty, S. Ghosh, A. Belanger, M. Sakthivel, T. S. Benefield, C. R. Inscoe, O. Zhou, J. Lu, and Y. Z. Lee, "Feasibility of a prototype carbon nanotube enabled stationary digital chest tomosynthesis system for identification of pulmonary nodules by pulmonologists," *Journal of Thoracic Disease*, vol. 14, no. 2, 2022, ISSN: 2077-6624. [Online]. Available: https://jtd.amegroups.com/article/view/61302.

[68] J. H. L. Goh, T. L. Tan, S. Aziz, and I. H. Rizuana, "Comparative study of digital breast tomosynthesis (dbt) with and without ultrasound versus breast magnetic resonance imaging (mri) in detecting breast lesion," *International Journal of Environmental Research and Public Health*, vol. 19, no. 2, 2022, ISSN: 1660-4601. DOI: 10.3390/ijerph19020759. [Online]. Available: https://www.mdpi.com/1660-4601/19/2/759.

[69] M. Opitz, S. Zensen, K. Breuckmann, D. Bos, M. Forsting, O. Hoffmann, M. Stuschke, A. Wetter, and N. Guberina, "Breast radiation exposure of 3d digital breast tomosynthesis compared to full-field digital mammography in a clinical follow-up setting," *Diagnostics*, vol. 12, no. 2, 2022, ISSN: 2075-4418. DOI: 10.3390/diagnostics12020456. [Online]. Available: https://www.mdpi.com/2075-4418/12/2/456.

[70] T. Gomi, Y. Kijima, T. Kobayashi, and Y. Koibuchi, "Evaluation of a generative adversarial network to improve image quality and reduce radiation-dose during digital breast tomosynthesis," *Diagnostics*, vol. 12, no. 2, 2022, ISSN: 2075-4418. DOI: 10.3390/diagnostics12020495. [Online]. Available: https://www.mdpi.com/2075-4418/12/2/495.